

An End-to-end Supervised Domain Adaptation Framework for Cross-Domain Change Detection

Jia Liu^{a,c,†}, Wenjie Xuan^{b,c,d,e,†}, Yuhang Gan^{b,c,d,e,f}, Juhua Liu^{a,c*}, Bo Du^{b,c,d,e}

^a Research Center for Graphic Communication, Printing and Packaging, Wuhan University, Wuhan, China.

^b National Engineering Research Center for Multimedia Software, Wuhan University, Wuhan, China.

^c Institute of Artificial Intelligence, Wuhan University, Wuhan, China.

^d School of Computer Science, Wuhan University, Wuhan, China.

^e Hubei Key Laboratory of Multimedia and Network Communication Engineering, Wuhan University, Wuhan, China.

^f Land Satellite Remote Sensing Application Center, MNR, Beijing, China.

Abstract. Change Detection is a crucial but extremely challenging task of remote sensing image analysis, and much progress has been made with the rapid development of deep learning. However, most existing deep learning-based change detection methods try to elaborately design complicated neural networks with powerful feature representations, but ignore the universal domain shift induced by time-varying land cover changes, including luminance fluctuations and season changes between pre-event and post-event images, thereby producing sub-optimal results. In this paper, we propose an end-to-end Supervised Domain Adaptation framework for cross-domain Change Detection, namely SDACD, to effectively alleviate the domain shift between bi-temporal images for better change predictions. Specifically, our SDACD presents collaborative adaptations from both image and feature perspectives with supervised learning. Image adaptation exploits generative adversarial learning with cycle-consistency constraints to perform cross-domain style transformation, effectively narrowing the domain gap in a two-side generation fashion. As to feature adaptation, we extract domain-invariant features to align different feature distributions in the feature space, which could further reduce the domain gap of cross-domain images. To further improve the performance, we combine three types of bi-temporal images for the final change prediction, including the initial input bi-temporal images and two generated bi-temporal images from the pre-event and post-event domains. Extensive experiments and analyses on two benchmarks demonstrate the effectiveness and universality of our proposed framework. Notably, our framework pushes several representative baseline models up to new State-Of-The-Art records, achieving 97.34% and 92.36% on the CDD and WHU building datasets, respectively. The source code and models are publicly available at <https://github.com/Perfect-You/SDACD>.

Keywords: Change Detection, Supervised Domain Adaptation, Image Adaptation, Feature Adaptation.

[†] **Jia Liu and Wenjie Xuan contributed equally to this work.**

Address all correspondence to:

* Juhua Liu, Research Center for Graphic Communication, Printing and Packaging, Wuhan University, Wuhan, China; Tel: +86-18062452253; E-mail: liuhuhua@whu.edu.cn.

1 Introduction

Change Detection (CD) aims to identify significant differences of geographical elements between bi-temporal images of the same geographic area, which takes registered bi-temporal images as the input and outputs pixel-wise change maps. This fundamental but important remote sensing task has gradually become an active topic in the computer vision community due to its wide applications in urbanization monitoring [1], resource and environment monitoring [2], disaster assessment [3], *etc.* Many excellent methods have been proposed recently thanks to the easy acquisition of high-resolution remote sensing images and the success of deep learning. However, many issues in this task remain open and challenging due to the complex and heterogeneous appearance of geographical elements at different times.

During the past decades, numerous kinds of conventional change detection methods have been proposed, which can be classified into four categories: 1) **Algebra-based methods** perform channel-wise algebraic operations on the registered bi-temporal images directly, including image differencing, image regression, change vector analysis [4], *etc.* But it is scene-dependent and time-consuming to find a suitable threshold to distinguish changed pixels from unchanged ones. 2) **Transformation-based methods** intend to cast bi-temporal images into specific feature spaces, capable of narrowing the pixel differences of unchanged regions and highlighting the changed information. However, such methods like [5]-[7] struggle to handle high-resolution images because of depending on empirically designed features. 3) **Classification-based methods** as [8][9] identify change regions by comparing the pre-generated land cover labels of geographic elements between bi-temporal images. However, the classification errors of the pre-generated labels would accumulate to the final change maps and inevitably reduce the accuracy of change predictions. 4) **Machine learning-based methods** employ classical traditional machine learning algorithms, such as random forest regression [10], support vector machine [11], and decision tree [12] to discriminate whether the specified area has changed. Although most of these conventional methods are simple and explainable, they show poor robustness in real senses because their performance is tolerant to noise and limited by hand-crafted features.

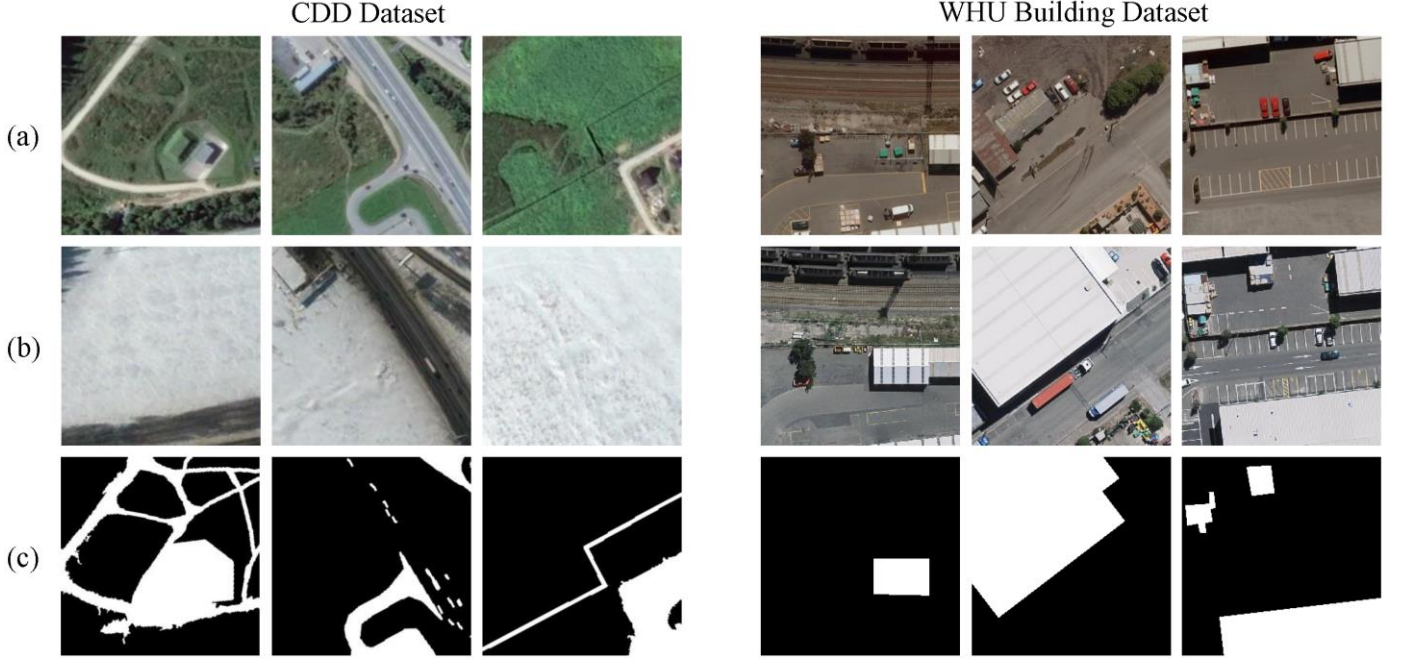


Fig. 1 The cross-domain bi-temporal images in the CDD and WHU building datasets. Images from top to bottom are (a) pre-event images, (b) post-event images, and (c) corresponding ground truths, respectively. The bi-temporal images of CDD dataset were acquired in summer and winter, while WHU building dataset was taken under varied luminance conditions in 2012 and 2016, respectively. Both datasets exhibit significant appearance variations.

Recently, benefiting from the rapid development of deep learning, many deep learning-based change detection methods have been proposed, and due to the powerful ability of automatic high-level feature extraction, they have demonstrated superior performance and robustness than conventional methods. Deep learning-based methods usually first extract discriminative features from bi-temporal images using convolutional neural networks similar to siamese networks, and then utilize fully convolutional networks or metric-based modules to predict the final change results[13]-[24]. Theoretically, for accurately predicting change results from the feature space, the features extracted from bi-temporal images should satisfy the following constraints: feature vectors associated with changed pixel pairs are farther apart from each other, while invariant pixel pairs are close. However, this assumption is hard to be satisfied in reality. Since the bi-temporal images are usually acquired at different times, their imaging sensors, atmospheric and luminance conditions would be different, which inevitably leads to completely different appearances in the bi-temporal images regardless of whether the geographical elements changed or not. As shown in Fig. 1, the time-varying changes introduced by seasons and climates are more obvious than the real ones caused by human factors,

such as the construction or destruction of buildings and roads. These pseudo-changes make it difficult for existing deep learning-based methods, which usually focus on designing complicated neural networks with powerful feature representation while ignoring the domain shift between bi-temporal images, to extract features satisfying the above constraints from the bi-temporal images.

In this paper, we propose a Supervised Domain Adaptation framework for cross-domain Change Detection, namely SDACD, to effectively alleviate the severe domain shift between the pre-event and post-event images. Our proposed SDACD presents collaborative adaptations from both image and feature perspectives, and comprises two key modules: Image Adaptation (IA) module and Feature Adaptation (FA) module. Image adaptation module addresses domain shift by aligning the image appearance between bi-temporal domains via image-to-image transformation. Specifically, we transform the appearance of pre-event images and post-event images to each other by using bi-directional generative adversarial networks with cycle-consistency constraints, *i.e.*, transform pre-event images to the appearance of post-event images, while post-event images to pre-event images. Afterwards, we employ two types of bi-temporal images from the pre-event domain and post-event domain as well as the original bi-temporal images to train the change detection model in the feature adaptation module, where we integrate feature adaptation into the framework to further narrow the remaining domain shift. Specifically, we first input three bi-temporal images, *i.e.*, the pre-event and post-event images, pre-event and post-event stylized as pre-event images, and post-event and pre-event stylized as post-event images, into feature adaptation module, and predict change map for each pair of bi-temporal images. Then we design a feature domain-invariant discriminator, which connects the change predictions and the bi-temporal images, to differentiate the predictions generated from which bi-temporal images. If this discriminator fails to distinguish, it means the extracted features for predicting change maps is domain-invariant. Finally, to fully utilize the image information from different domains, we make the final change prediction by fusing the above three features from different bi-temporal images. Our proposed framework combines the image and feature adaptation procedures in an end-to-end trainable manner, which can make them benefit from each other and achieve better performance. To the best of our knowledge, it is the first

work that fully studies domain adaptation with supervised learning for change detection, and provides a simple and effective solution that can be easily plugged in any non-domain adaptation models to further improve their performance. The architecture of our proposed framework is shown in Fig. 2.

We implement SDACD framework based on three representative baseline models, STANet [14], DASNet [15], and SNUNet [16], respectively, and validate the effectiveness and universality of our framework on the CDD [25] and WHU building datasets [26]. Our framework shows consistent improvements on all three baseline models. For the CDD dataset, the *F1-score* of STANet, DASNet and SNUNet-based frameworks improves by 0.70%, 0.78% and 1.66%, respectively, while for WHU building dataset, it improves by 8.81%, 2.59% and 6.85%, respectively. Moreover, combined with the cutting-edge SNUNet, our framework achieves the State-Of-The-Art performance on both datasets. Visualized results also demonstrate the superiority of our framework in dealing with bi-temporal change detection under severe domain shifts as illustrated in Section 4.

Our contributions can be summarized in three folds:

- We propose a novel supervised domain adaptation framework SDACD for cross-domain change detection, which unifies image adaptation and feature adaptation in an end-to-end trainable manner to alleviate the domain shift between the pre-event and post-event images;
- Our framework is compatible with existing change detection networks which take no consideration of domain shifts, and it can handle cross-domain change detection and consistently improve the performance as an easy-to-plug-in module;
- Experimental results on two benchmark datasets demonstrate the effectiveness and universality of our SDACD. Most importantly, our SNUNet-based framework sets new state-of-the-art performance with an *F1-score* of 97.34% on CDD dataset and 92.36% on WHU building dataset.

The rest of the paper is organized as follows. In Section 2, we briefly review the related works of change detection and domain adaptation. In Section 3, we introduce our proposed framework before analyzing each module. Section 4 reports and discusses the experiment results. Finally, we conclude in Section 5.

2 Related Works

2.1 Change detection

In recent years, due to the powerful feature extraction capabilities of deep neural networks, many deep learning-based change detection methods have been proposed, which can be divided into two main categories, *i.e.*, patch-based methods and image-based methods.

Patch-based methods [27]-[30] regard patch as the smallest processing unit for change detection. These methods first split bi-temporal images into patches, and then discriminate for each patch whether it has changed or not. Zhang et al. [27] employed a deep belief network to transform multi-spectral image patches into specified feature spaces and relieve noise for change detection. To facilitate the utilization of spectral-spatial-temporal representations, Mou et al. [28] designed a ReCNN, which combined CNNs with RNNs to explore spectral-spatial representations and temporal dependencies between the patches of bi-temporal images. Although patch-based methods have made remarkable progress compared with traditional methods, they suffer from high memory consumption and low computational efficiency. Furthermore, patch size restricts the receptive field, thus these methods cannot exploit global information, which also greatly limits their performance.

Image-based methods [14]-[24], [31]-[33] directly employ the whole image to make pixel-wise predictions, which is computation-efficient and well-performed. FC-EF, FC-Siam-conc, and FC-Siam-diff [17] are some earlier image-based methods. These methods employed UNet [34] as the backbone network of feature extractors and explored three different feature fusion strategies, which greatly improved the performance and processing speed compared to patch-based methods. Later, Chen et al. [14] proposed an influential STANet, which designed a spatial-temporal self-attention module in the siamese network to explore spatial-temporal dependencies between bi-temporal images. Recently, Fang et al. [16] proposed a densely connected SNUNet and achieved SOTA on the CDD dataset. SNUNet adopted a siamese UNet++ [35] architecture as the feature extractor and utilized an ensemble channel attention module to aggregate multi-level features for enhancing discriminative feature representations.

However, though aforementioned methods have achieved inspiring results by powerful feature extractors and elaborately designed structures, few methods consider the universal domain shift between bi-temporal images caused by different seasons, various imaging conditions, etc., thus producing sub-optimal results. DLSF [36] and PDA [37] are recent representative methods for cross-domain change detection, which employed GAN [38] with complex constraints to preserve semantic information and bridge the style gaps between bi-temporal images. Our method differs from DLSF and PDA in two folds. First, these two methods only employ image adaptation with complex constraints, but we alleviate domain shift from both image and feature perspective, and validate the effectiveness of each component. Second, they are specially designed for metric-based predictors, while our SDACD is compatible with most existing deep learning-based methods.

2.2 Domain adaptation

Domain adaptation intends to address performance degradation caused by domain shift by transferring knowledge between domains, which benefits the generalization of models. Given the source domain and target domain, most of the existing methods consider the unsupervised or semi-supervised situation, where no or only limited labels in the target domain are available. To our knowledge, domain adaptation mainly focuses on two aspects, *i.e.*, image adaptation and feature adaptation.

Image adaptation attempts to minimize appearance differences for images of different modals or styles. An intuitive idea is to transform images from one style to another through generation models. The famous CycleGAN [39] first employed bi-directional generation with cycle-consistency constraints in GAN and realizes desirable unpaired image-to-image transformation, which provided a reference paradigm for image adaptation. Afterwards, many works apply the ideas of CycleGAN to deal with domain shift via image-to-image transformation. For example, CyCADA [40] first employed a cycle-consistent GAN to transform source domain images to target domain, and then train the model with the synthetic data in the target domain. On the contrary, Song et al. [41] transformed target domain images into the source domain, then generated pseudo-labels using the source domain model, and finally utilized them to fine-tune source domain model.

Feature adaptation aligns the feature distributions between the source and target domain by exploiting

domain-invariant features acquired by adversarial training. DANN [42] was the earliest general framework that employs adversarial training to learn domain-invariant features for domain adaptation. To further improve the discrimination of domain-invariant features, Tzeng et al. [43] combined discriminative models with an untied weight sharing strategy. Furthermore, Wang et al. [44] considered the transferability of features in each domain and proposed a well-designed attention module to select suitable representations for feature adaptation.

As mentioned above, most existing domain adaptation methods are designed for unsupervised or semi-supervised scenes, while we treat cross-domain change detection as a supervised domain adaptation problem, where there are supervised annotations for bi-temporal images with severe domain shift. Though current methods provide valuable solutions to bridge domain gaps, they would suffer from underutilization or loss of image information in cross-domain change detection. Our work is closely related to SIFA [45], which also combined image adaptation and feature adaptation for domain adaptation. However, SIFA aims to recover performance degradation when transferring the segmentation models from MR images to CT images. We highlight that our work focuses on increasing the performance of change detection by relieving the domain shift between bi-temporal images under supervised settings. The main contribution of our work is providing a general change detection framework, which can enhance the performance of existing change detection methods by adopting the ideas of domain adaptation.

3 Methodology

In this section, we first introduce the overview architecture of our proposed framework, and then illustrate details of two main modules: the image adaptation module and the feature adaptation module. Finally, we define the full loss function of our framework.

3.1 Overall Architecture

Fig. 2 depicts the overall architecture of our proposed framework. Given the pre-event image $I_{pre} \in R^{H \times W \times C}$ and the post-event image $I_{post} \in R^{H \times W \times C}$, our framework aims to predict a binary change map $O \in R^{H \times W}$, $\{o_i \in O | o_i \in \{0, 1\}, i = 1, 2, \dots, HW\}$, where 1 represents changed pixel and 0 means no

change. To highlight the cross-domain change detection problem, we denote the pre-event image $I_{pre} \in PrD$ and the post-event image $I_{post} \in PoD$ ($PrD \neq PoD$), where PrD and PoD represent the pre-event domain and post-event domain, respectively.

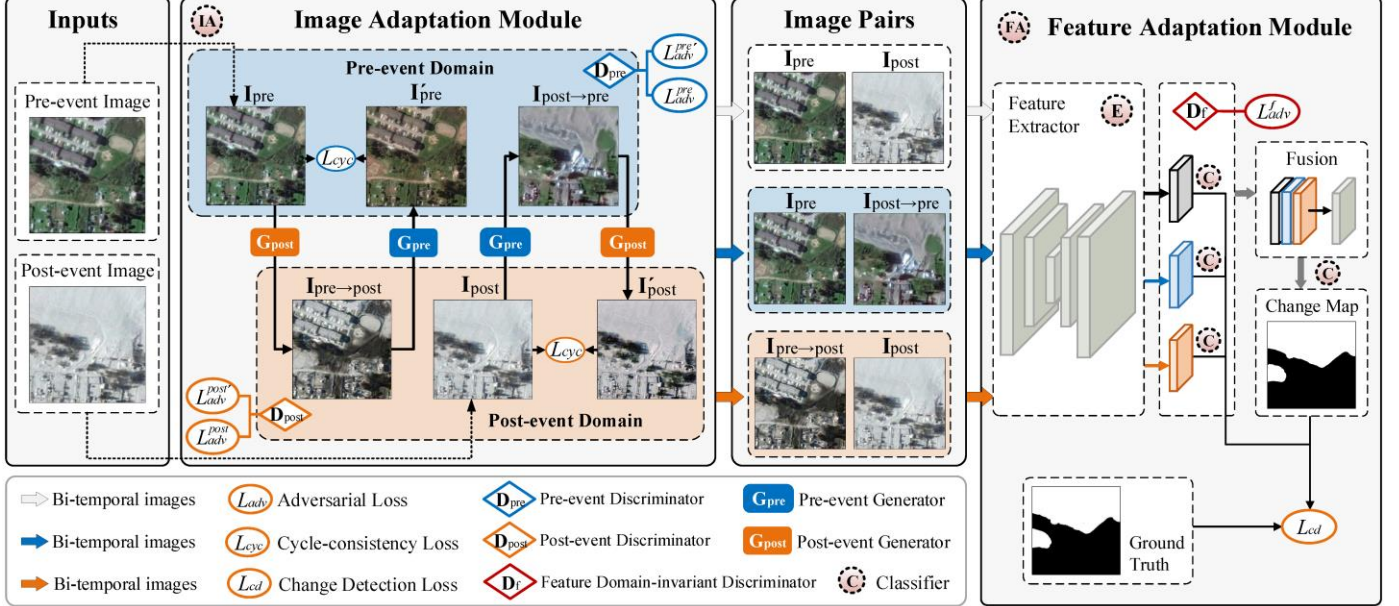


Fig. 2 The overall architecture of our SDACD framework for cross-domain change detection. Given bi-temporal images (I_{pre}, I_{post}) with severe domain shift, we first utilize an image adaptation module (IA) to alleviate the domain shift by aligning image appearance. Then we input two bi-temporal images from the pre-event domain and post-event domain, *i.e.*, ($I_{pre}, I_{post \rightarrow pre}$) and ($I_{pre \rightarrow post}, I_{post}$), as well as the original bi-temporal images (I_{pre}, I_{post}) into feature adaptation module (FA), and extract domain-invariant features via a feature domain-invariant discriminator. Feature adaptation module can further reduce domain gap by aligning feature distributions from different domains in feature space. Finally, we integrate the extracted features from three bi-temporal images to predict the final change map by the classifier C . Better viewed in color.

In order to narrow the domain gap, we design an Image Adaptation (IA) module and a Feature Adaptation (FA) module to implement domain adaptation from different perspectives. Accordingly, the pipeline can be divided into two main phases. Firstly, we transform the pre-event image I_{pre} to the post-event domain PoD for obtaining the pre-event stylized as post-event image $I_{pre \rightarrow post}$. Meanwhile, we generate the post-event stylized as pre-event image $I_{post \rightarrow pre}$ by transforming the post-event image I_{post} to the pre-event domain PrD . Therefore, we obtain two bi-temporal images in the same domain, where $(I_{pre}, I_{post \rightarrow pre}) \in PrD$, $(I_{pre \rightarrow post}, I_{post}) \in PoD$. Afterwards, we input the two generated bi-temporal images ($I_{pre}, I_{post \rightarrow pre}$), ($I_{pre \rightarrow post}, I_{post}$) with the original (I_{pre}, I_{post}) into the feature adaptation module, where we further reduce

domain gap by aligning feature distributions in feature space via a feature domain-invariant discriminator. Finally, for fully utilizing the image information from different domains, we predict the final change map O by fusing the aligned features that extracted from the above three bi-temporal images. More details of IA and FA modules will be revealed in the following sections.

3.2 Image Adaptation Module for Appearance Alignment

Since bi-temporal images are usually captured under different imaging conditions, we specifically design an Image Adaptation (IA) module to minimize the appearance variations between bi-temporal images while the original contents with geographical semantics remain unaffected. The goal of IA module is to learn mapping functions between two domains PrD and PoD given training samples (I_{pre}, I_{post}) .

As shown in Fig. 2 (IA), we employ generative adversarial networks, which have made wide success for image-to-image transformation, by building two generators $G_{pre}: I_{post} \rightarrow I_{pre}$ and $G_{post}: I_{pre} \rightarrow I_{post}$, and two adversarial discriminators D_{pre} and D_{post} . The generator G_{pre} aims to transform images in the post-event domain to the pre-event domain, while G_{post} performs reverse image transformation. The discriminators D_{pre} and D_{post} compete with their corresponding generators to correctly distinguish the real images from the transformed ones. Therefore, the generator G_{pre} and its discriminator D_{pre} can be optimized via the adversarial learning:

$$\begin{aligned} \mathcal{L}_{adv}^{pre}(G_{pre}, D_{pre}, PoD, PrD) = & \mathbb{E}_{I_{pre} \sim PrD} [\log D_{pre}(I_{pre})] + \\ & \mathbb{E}_{I_{post} \sim PoD} [\log(1 - D_{pre}(G_{pre}(I_{post})))] \end{aligned} \quad (1)$$

where G_{pre} aims to generate images $G_{pre}(I_{post})$ that have similar appearance to images from the pre-event domain PrD , while D_{pre} tries to distinguish real images I_{pre} from transformed images $G_{pre}(I_{post})$. G_{pre} aims to minimize this objective against D_{pre} that tries to maximize it, *i.e.*, $\min_{G_{pre}} \max_{D_{pre}} \mathcal{L}_{adv}^{pre}(G_{pre}, D_{pre}, PoD, PrD)$. Similarly, the adversarial loss for the generator G_{post} and its discriminator D_{post} can be defined as:

$$\mathcal{L}_{adv}^{post}(G_{post}, D_{post}, PrD, PoD) = \mathbb{E}_{I_{post} \sim PoD} [\log D_{post}(I_{post})] +$$

$$\mathbb{E}_{I_{pre} \sim PrD} [\log(1 - D_{post}(G_{post}(I_{pre})))] \quad (2)$$

Same as CycleGAN[39], we also employ a reverse generator to impose pixel-wise cycle-consistency for preserving original geographical elements in the transformed images. As shown in Fig. 2 (IA), for each image I_{pre} from domain PrD , the image transformation cycle should be able to bring I_{pre} back to the original image, *i.e.*, $I_{pre} \rightarrow G_{post}(I_{pre}) = I_{pre \rightarrow post} \rightarrow G_{pre}(G_{post}(I_{pre})) = I_{pre \rightarrow post \rightarrow pre} \approx I_{pre}$. Similarly, for each image I_{post} from PoD , G_{pre} and G_{post} should also satisfy cycle-consistency: $I_{post} \rightarrow G_{pre}(I_{post}) = I_{post \rightarrow pre} \rightarrow G_{post}(G_{pre}(I_{post})) = I_{post \rightarrow pre \rightarrow post} \approx I_{post}$. The cycle-consistency loss \mathcal{L}_{cyc} can be computed as follows:

$$\begin{aligned} \mathcal{L}_{cyc}(G_{pre}, G_{post}) = & \mathbb{E}_{I_{pre} \sim PrD} [||G_{pre}(G_{post}(I_{pre})) - I_{pre}||_1] + \\ & \mathbb{E}_{I_{post} \sim PoD} [||G_{post}(G_{pre}(I_{post})) - I_{post}||_1] \end{aligned} \quad (3)$$

Since our image transformation procedures are cycle, we also introduce two reverse adversarial loss $\mathcal{L}_{adv}^{pre'}$ and $\mathcal{L}_{adv}^{post'}$ for the two reverse image transformations, *i.e.*, $I_{pre \rightarrow post} \rightarrow I_{pre \rightarrow post \rightarrow pre} \approx I_{pre}$ and $I_{post \rightarrow pre} \rightarrow I_{post \rightarrow pre \rightarrow post} \approx I_{post}$. The reverse adversarial losses $\mathcal{L}_{adv}^{pre'}$ and $\mathcal{L}_{adv}^{post'}$ can be computed as follows:

$$\begin{aligned} \mathcal{L}_{adv}^{pre'}(G_{pre}, D_{pre}, PoD, PrD) = & \mathbb{E}_{I_{pre} \sim PrD} [\log D_{pre}(I_{pre})] + \\ & \mathbb{E}_{I_{pre \rightarrow post} \sim PoD} [\log(1 - D_{pre}(G_{pre}(I_{pre \rightarrow post})))] \end{aligned} \quad (4)$$

$$\begin{aligned} \mathcal{L}_{adv}^{post'}(G_{post}, D_{post}, PrD, PoD) = & \mathbb{E}_{I_{post} \sim PoD} [\log D_{post}(I_{post})] + \\ & \mathbb{E}_{I_{post \rightarrow pre} \sim PrD} [\log(1 - D_{post}(G_{post}(I_{post \rightarrow pre})))] \end{aligned} \quad (5)$$

Therefore, the full adversarial loss of image adaptation \mathcal{L}_{adv}^i can be formulated as:

$$\begin{aligned} \mathcal{L}_{adv}^i(G_{pre}, D_{pre}, G_{post}, D_{post}, PrD, PoD) = & \mathcal{L}_{adv}^{pre}(G_{pre}, D_{pre}, PoD, PrD) + \\ & \mathcal{L}_{adv}^{post}(G_{post}, D_{post}, PrD, PoD) + \\ & \mathcal{L}_{adv}^{pre'}(G_{pre}, D_{pre}, PoD, PrD) + \end{aligned}$$

$$\mathcal{L}_{adv}^{post'}(G_{post}, D_{post}, PrD, PoD) \quad (6)$$

3.3 Feature Adaptation Module for Feature Alignment

After the original bi-temporal images (I_{pre}, I_{post}) is transformed by the above image adaptation module, we can obtain several bi-temporal images. Ideally, we can train a change detection model with excellent performance by using bi-temporal images ($I_{pre}, I_{post \rightarrow pre}$) or ($I_{pre \rightarrow post}, I_{post}$) from the domain PrD or PoD . However, for training a cross-domain change detection model with optimal performance, several challenges remain to be solved. Firstly, for bi-temporal images of cross-domain remote sensing, due to the severe domain shift between bi-temporal images, only utilizing image adaptation would be insufficient to achieve the expected domain adaptation results. Secondly, during the image adaptation procedure, compared with the original image, the generated image has the issue of information loss more or less. Therefore, using only one domain bi-temporal images to train change detection model would also suffer from underutilization or even loss of image information, thus producing sub-optimal results.

To this end, we design a Feature Adaptation (FA) module to further reduce the remaining domain gap and fully utilize the image information from different domains. For further reducing the remaining domain gap, we impose an additional feature domain-invariant discriminator to align feature distributions in feature space and contribute from the perspective of feature adaptation. Generally speaking, feature adaptation aims to extract domain-invariant features without considering the appearance difference between input domains. The most intuitive way is to use a discriminator to distinguish which features come from which domain via adversarial learning. However, since the feature space is high-dimensional, it is difficult to directly align using adversarial learning. Inspired by output space adaptation [46], we enhance the domain-invariance of feature distribution via adversarial learning in the different lower-dimensional spaces. Specifically, we add adversarial losses between the change detection prediction space and the input bi-temporal image spaces.

As shown in Fig. 2 (FA), we adopt three bi-temporal images from different domains, including (I_{pre}, I_{post}) $\in PrD$, ($I_{pre}, I_{post \rightarrow pre}$) $\in PoD$ and the initial bi-temporal images ($I_{pre \rightarrow post}, I_{post}$), to train the change

detection model. We make change predictions for each bi-temporal images and construct a feature domain-invariant discriminator D_f to differentiate whether the predictions come from (I_{pre}, I_{post}) , $(I_{pre}, I_{post \rightarrow pre})$ or $(I_{pre \rightarrow post}, I_{post})$. If the features extracted from different domains are aligned, discriminator D_f would fail to differentiate their corresponding predictions. Otherwise, the adversarial gradients are back-propagated into the feature extractor E of bi-temporal images to minimize the distance among the feature distributions from different domains. Since there are three input bi-temporal images, there are three adversarial losses for feature adaptation, which can be computed as:

$$\begin{aligned} \mathcal{L}_{adv}^f(I_{pre}, I_{post}, C, E, D_f) &= \mathbb{E}[\log D_f(C(E(I_{pre}), E(I_{post})))]) + \\ &\quad \mathbb{E}[\log(1 - D_f(C(E(I_{pre}), E(I_{post})))]) \end{aligned} \quad (7)$$

$$\begin{aligned} \mathcal{L}_{adv}^f(I_{pre \rightarrow post}, I_{post}, C, E, D_f) &= \mathbb{E}[\log D_f(C(E(I_{pre \rightarrow post}), E(I_{post})))]) + \\ &\quad \mathbb{E}[\log(1 - D_f(C(E(I_{pre \rightarrow post}), E(I_{post})))]) \end{aligned} \quad (8)$$

$$\begin{aligned} \mathcal{L}_{adv}^f(I_{pre}, I_{post \rightarrow pre}, C, E, D_f) &= \mathbb{E}[\log D_f(C(E(I_{pre}), E(I_{post \rightarrow pre})))]) + \\ &\quad \mathbb{E}[\log(1 - D_f(C(E(I_{pre}), E(I_{post \rightarrow pre})))]) \end{aligned} \quad (9)$$

where C represents classifier for change prediction.

Combined with the above three adversarial losses, the full adversarial loss of feature adaptation \mathcal{L}_{adv}^f can be formulated as:

$$\begin{aligned} \mathcal{L}_{adv}^f(C, E, D_f) &= \mathcal{L}_{adv}^f(I_{pre}, I_{post}, C, E, D_f) + \\ &\quad \mathcal{L}_{adv}^f(I_{pre \rightarrow post}, I_{post}, C, E, D_f) + \\ &\quad \mathcal{L}_{adv}^f(I_{pre}, I_{post \rightarrow pre}, C, E, D_f) \end{aligned} \quad (10)$$

As mentioned above, the generated images from image adaptation would suffer more or less information loss, which results in sub-optimal model trained with bi-temporal image samples from only one domain. Therefore, for fully utilizing the image information from different domains and keeping training samples diverse, we integrate the aligned features, which are extracted from (I_{pre}, I_{post}) , $(I_{pre}, I_{post \rightarrow pre})$ and

$(I_{pre \rightarrow post}, I_{post})$ to predict the final change map O . We also conduct ablation studies to investigate the selection of bi-temporal images for training change detection model and fusion strategies for prediction final change map, which will be discussed in Section 4.4.2 and Section 4.4.3, respectively.

During feature adaptation procedure, we make change predictions for each input bi-temporal images, and then fuse the aligned features to predict the final change map. Therefore, the full change detection loss \mathcal{L}_{CD} can be computed as follows:

$$\mathcal{L}_{CD} = \sum_{i=0,1,2} \mathcal{L}(\hat{O}_i, Y) + \mathcal{L}(O, Y) \quad (11)$$

where i is the index of input bi-temporal images, \hat{O}_i is the prediction result of the i -th bi-temporal images during feature adaptation, O is final prediction result of our framework, Y is the ground truth, and $\mathcal{L}(\cdot)$ is the loss function of the baseline change detection model adopted in our framework.

3.4 Full Objective

The key characteristic of SDACD is that both image and feature adaptations are unified into an end-to-end trainable framework. At each training iteration, the key modules are sequentially updated as following order:

$G_{pre} \rightarrow G_{post} \rightarrow D_{pre} \rightarrow D_{post} \rightarrow E \rightarrow C \rightarrow D_f \rightarrow C$. Specifically, in the image adaptation module, the generators G_{pre} and G_{post} are updated first to transform I_{post} and I_{pre} into generated pre-event and post-event images, *i.e.*, $I_{post \rightarrow pre}$ and $I_{pre \rightarrow post}$, respectively. Then the discriminators D_{pre} and D_{post} are updated to distinguish the real images from generated images. Next, the feature extractor E in the feature adaptation module is updated to extract features from the three input bi-temporal images, and then the change predictor C is updated to predict change maps for each bi-temporal images based on the extracted features. Afterward, the feature domain-invariant discriminator D_f is updated to distinguish the input domain of the three prediction maps. Finally, the change predictor C is updated to predict the final change map based on the fused features. Therefore, combined with the cycle-consistency loss and adversarial loss of image adaptation in Eq. (3) and Eq. (6), the full adversarial loss of feature adaptation in Eq. (10) and the change detection loss in Eq. (11), the full multi-task loss function can be defined as:

$$\mathcal{L} = \mathcal{L}_{cyc} + \mathcal{L}_{adv}^i + \mathcal{L}_{adv}^f + \mathcal{L}_{CD} \quad (12)$$

4 Experiments

In this section, we implement SDACD framework based on STANet (2020), DASNet (2021), and SNUNet (2021), respectively, and conduct experiment on the CDD and WHU building datasets which contain time-varying changes caused by seasons or luminance. We compare our method with the baseline as well as state-of-the-art methods, and carefully analyze the functions of each proposed module.

4.1 Datasets and Evaluation Metrics

CDD [25] is a widely-used dataset for change detection proposed by M.A et al., contains 11 pairs of bi-temporal images obtained from Google Earth in different seasons with a spatial resolution from 3 to 100 cm per pixel. Since the original bi-temporal images included seven 4725×2700 image pairs and four 1900×1000 image pairs, which were too large to process directly, the authors cropped the original image pairs into the same size of 256×256 pixels, thus generating 10000 image pairs for training, 3000 image pairs for validation, and 3000 image pairs for testing. As shown in Fig. 1, the appearances of bi-temporal images are varied greatly due to different seasons. To conform to the assumption $I_{pre} \in PrD$, $I_{post} \in PoD$ where $PrD \neq PoD$, we partially adjust the order of bi-temporal image pairs to obtain similar appearances in each domain, forming summer-styled pre-event images and winter-styled post-event images. The annotations of changed regions consist of objects varied in size and category, including cars, roads, constructions, etc.

WHU Building Dataset [26] mainly focuses on the changes of buildings, and contains one pair of very high-resolution images sized 32507×15354 pixels with a spatial resolution of 0.075m per pixel. Authors divided the original image pair into a training set of 21243×15354 pixels and a testing set of 11265×15354 pixels. Because of memory constraints, we further crop the images into patches of 256×256 pixels without overlap, producing 4980 bi-temporal images for training and 2700 bi-temporal images for testing. Note that images were taken in 2012 and 2016 separately, thus bi-temporal images showed varied appearances caused by luminance fluctuations, as shown in Fig. 1. The annotations only consist of changes caused by constructions and destructions of buildings.

We adopt three metrics to evaluate the performance of cross-domain change detection, including Precision (P), Recall (R), and *F1-score*. While Precision reflects the accuracy of detection, Recall represents the completeness of the predicted changed regions. Generally, *F1-score* is more concerned by researchers because it takes both Precision and Recall into account and reflects the comprehensive performance of the method.

4.2 Implementation details

Our experiments were conducted on the high-performance servers with NVIDIA Tesla V100 (16G) GPU. We implemented our framework SDACD based on three baseline models, denoted as STANet-SDACD, DASNet-SDACD, and SNUNet-SDACD. Following the original settings in [14][15][16], we initialized STANet and DASNet by public available pre-trained ImageNet parameters, while SNUNet is initialized by kaiming normalization. The other parameters are all initialized by kaiming normalization. For data augmentation, we employed random flips, random rotation, and normalization. In addition, since the proportion of changed areas is relatively small in WHU building dataset, we further augmented the training set with 3442 bi-temporal images generated by randomly cropping several 256×256 patches around each instance of changed areas. We adopted Adam optimizer, and the initial learning rates are set to 5e-4 in all experiments. We train STANet and STANet-SDACD for 200 epochs, DASNet and DASNet-SDACD for 60 epochs, and SNUNet and SNUNet-SDACD for 120 epochs. Note that all networks are trained in an end-to-end manner.

4.3 Comparison with State-of-the-Art Methods

4.3.1 Comparison Methods

To demonstrate the superiority of our framework, we compared the performance of our framework with several representative and state-of-the-art deep learning-based change detection methods.

FC-EF, **FC-Siam-conc** and **FC-Siam-diff** [17] are the earliest FCN-based methods, which integrated UNet into the siamese architecture for change detection. These three methods explored three different fusion

strategies including bi-temporal images fusion, multi-level feature concatenation, and multi-level feature difference, which are main strategies for bi-temporal feature fusion in existing change detection methods.

STANet [14] is an impressive work in recent years, which utilizes a pyramid transformer structure to learn multi-level spatial-temporal dependencies. This structure effectively eliminates wrong detections caused by luminance difference and misregistration.

DASNet [15] employed a siamese convolutional module to obtain local features of the images at different times and then builds connections between local features by a dual attention module, which exploited globally contextual information to distinguish the changed areas from the unchanged ones.

SNUNet [16] is the current state-of-the-art method on CDD dataset. It employed a UNet++ architecture to extract multi-level representations and designs an elaborate ensemble channel attention module (ECAM) to integrate multi-level features, which boosted the performance to a higher level.

4.3.2 Performance on CDD Dataset

The left column of Table 1 lists the experimental results on CDD dataset. Though STANet, DASNet, and SNUNet have already exhibited impressive performance, our SDACD-STANet, SDACD-DASNet, and SDACD-SNUNet can bring consistent improvements on *F1-score* by 0.7%, 0.78%, and 1.66%. Notably, based on the cutting-edge work SNUNet, our method achieves new state-of-the-art performance on CDD with *F1-score* of 97.34%. Our framework outperforms the baseline model mainly benefits from the consideration of domain adaptation from two perspectives. First, IA module aligns the image appearance by image-to-image transformation, which effectively relieves the effect of different seasons and climates on the land cover changes. Second, FA module further reduces the remaining domain shift by exploiting domain-invariant features to predict the final change map. Besides, the results in Table 1 also imply that the performance of other deep learning-based models also could be further enhanced by combining with our SDACD framework. Therefore, our framework shows great potential in cross-domain change detection as an easy-to-plug-in module, which provides a simple but effective way to tackle the performance degradation caused by different seasons and climates for existing non-domain adaptation models.

As shown in Fig. 3, since bi-temporal images have significantly different appearance (summer *vs.* winter), this poses great challenges for the baseline models, which takes no consideration of domain shift, to discriminate real changes from false positives, especially for those changed regions with delicate structures. However, our SDACD can minimize the impact of time-varying land cover changes, and accurately detect fine boundaries of roads and small-scale object changes, which explicitly demonstrate the superiority of our framework for cross-domain change detection.

Table 1. Performance comparison with the state-of-the-art methods on CDD and WHU building datasets. The **red** and **blue** arrows indicate the increase and decrease of metrics compared with the baseline model, respectively.

| Methods | CDD | | | WHU building | | |
|--------------|--|--|--|---|--|--|
| | P (%) | R (%) | F (%) | P (%) | R (%) | F (%) |
| FC-EF | 84.68 | 65.13 | 73.63 | 80.75 | 67.29 | 73.40 |
| FC-Siam-diff | 87.57 | 66.69 | 75.07 | 48.84 | 88.96 | 63.06 |
| FC-Siam-conc | 88.81 | 62.20 | 73.16 | 54.20 | 81.34 | 65.05 |
| STANet | 83.17 | 92.76 | 87.70 | 82.12 | 89.19 | 83.40 |
| SDACD-STANet | 87.40 ↑4.23 | 89.50 ↓3.26 | 88.40 ↑0.70 | 90.90 ↑8.78 | 93.50 ↑4.31 | 92.21 ↑8.81 |
| DASNet | 93.28 | 89.91 | 91.57 | 83.77 | 91.02 | 87.24 |
| SDACD-DASNet | 92.85 ↓0.43 | 91.87 ↑1.96 | 92.35 ↑0.78 | 89.21 ↑5.44 | 90.46 ↓0.56 | 89.83 ↑2.59 |
| SNUNet | 96.60 | 94.77 | 95.68 | 82.12 | 89.19 | 85.51 |
| SDACD-SNUNet | 97.13 ↑0.53 | 97.56 ↑2.79 | 97.34 ↑1.66 | 93.85 ↑11.73 | 90.91 ↑1.72 | 92.36 ↑6.85 |

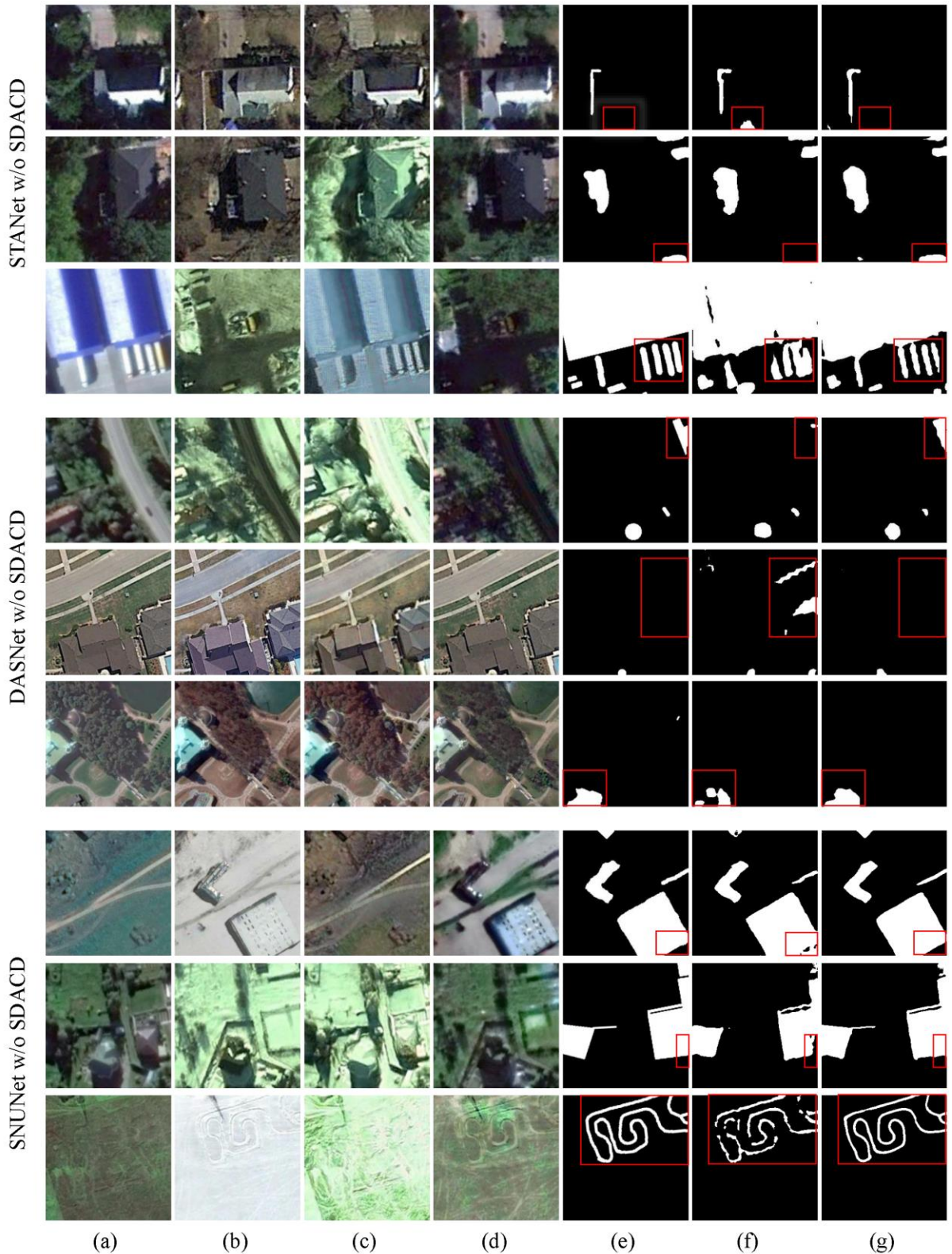


Fig. 3 Visualized experimental results on CDD. Images from left to right are (a) pre-event images, (b) post-event images, (c) pre-event stylized as post-event images, (d) post-event stylized as pre-event images, (e) ground truth, (f) the results of baseline, (g) the results of baseline + SDACD. Compared with the corresponding baselines, our method can effectively avoid false positive predictions introduced by varied seasons and climates, and preserve detailed changes with more clear boundaries.

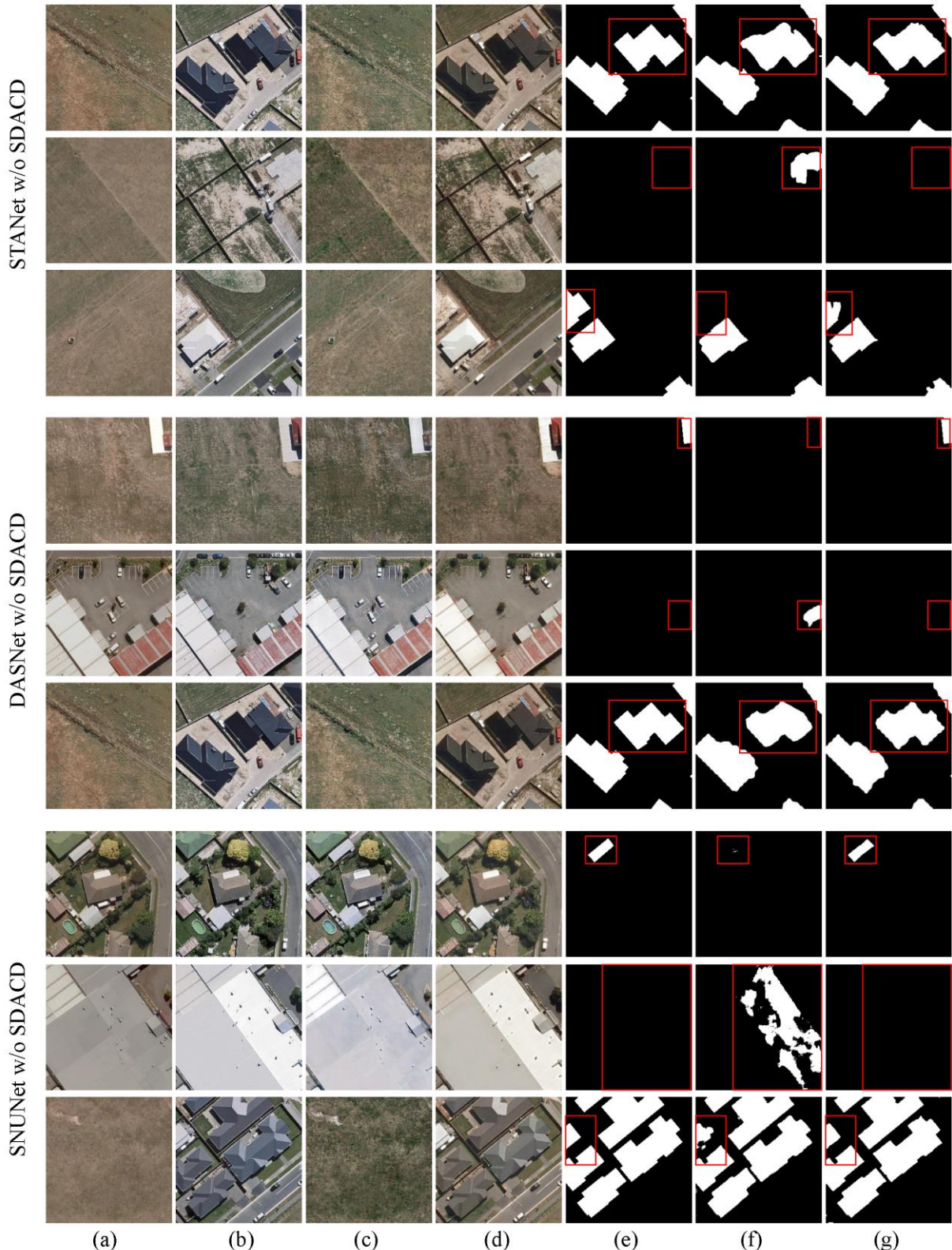


Fig. 4. Visualized experimental results on WHU Building Dataset. Images from left to right are (a) pre-event images, (b) post-event images, (c) pre-event stylized as post-event images, (d) post-event stylized as pre-event images, (e) ground truth, (f) the results of baseline, (g) the results of baseline + SDACD.

4.3.3 Performance on WHU Building Dataset

Different from CDD that is a class-agnostic change detection dataset, WHU building dataset focuses on building changes. Therefore, WHU building dataset is considered more challenging than CDD. We further conduct experiments on WHU building dataset to see if our framework can work under this more challenging scenery. We report the experimental results in the right column of Table 1. Similar to CDD, our framework outperforms the baseline model by a large margin, bringing an increment on *F1-score* of 8.81% on STANet, 2.59% on DASNet, and 6.85% on SNUNet. Moreover, our SDACD-SNUNet also achieves new state-of-the-art performance on the WHU building dataset with an *F1-score* of 92.36%. Such experimental results further verify that our framework can not only effectively bridge the appearance difference by image adaptation, but also provide domain-invariant and discriminative representations, which are significant for the precision of change detection.

Visual comparison results are provided in Fig. 4. We notice that without domain adaptation, the baseline models are prone to pseudo-changes caused by luminance fluctuations. In contrast, since our framework provides the domain adaptation ability to the baseline model, it helps to avoid false positives and false negatives, thus generating more precise change predictions with clear boundaries and enhancing the performance of cross-domain change detection.

4.4 Ablation Study

In this section, we conduct ablation studies on WHU building dataset to evaluate the effectiveness of each component proposed in SDACD based on SNUNet. In addition, we also reveal the insights into the framework design, *i.e.*, why we employ such three bi-temporal images for feature extraction and which strategy is the best for fusing feature maps from different domains.

4.4.1 Effectiveness of IA and FA Modules

We first conduct experiments to verify the effectiveness of the proposed IA and FA modules. The experimental results are reported in Table 2 and demonstrate both IA module and FA module improve the performance of the baseline model by a large margin. Specifically, with the help of IA module, our framework

remarkably improves the precision by 9.73%, which contributes most to the improvement of *F1-score*. As shown in Fig. 5, this is because our IA module can relieve the appearance difference between bi-temporal images and effectively avoid most of false positives produced by the baseline model. Moreover, it can be observed that incorporating FA module with IA module achieves the best performance with a competitive recall value and an improvement of 2% on precision. The reason is that, as described in Section 3.3, image adaptation alone is insufficient for the optimal results due to severe domain shift between bi-temporal images and more or less information loss during image-to-image transformation. Thus, FA module further improves the performance by exploiting domain-invariant features to alleviate the domain gap from another perspective. Visualized results in Fig. 6 also reveal similar observations. Therefore, we can conclude that our proposed adaptation modules, *i.e.*, IA and FA, are both effective in boosting the cross-domain change detection performance.

Table 2. Impact of the proposed IA and FA modules on WHU building dataset.

| Baseline | IA | FA | P (%) | R (%) | F (%) |
|----------|----|----|--------------|--------------|--------------|
| SNUNet | | | 82.12 | 89.19 | 85.51 |
| | ✓ | | 91.85 | 91.10 | 91.47 |
| | ✓ | ✓ | 93.85 | 90.91 | 92.36 |

Fig. 5. The results of cross-domain image-to-image transformation through IA module. Images from top to bottom are (a) pre-event images, (b) pre-event stylized as post-event images, (c) post-event images, (d) post-event stylized as pre-event images. Note

that images of (a) and (d) belong to the pre-event domain, while (b) and (c) belong to the post-event domain. The transformed images in the same domain share similar appearance, which validates the effectiveness of IA module.

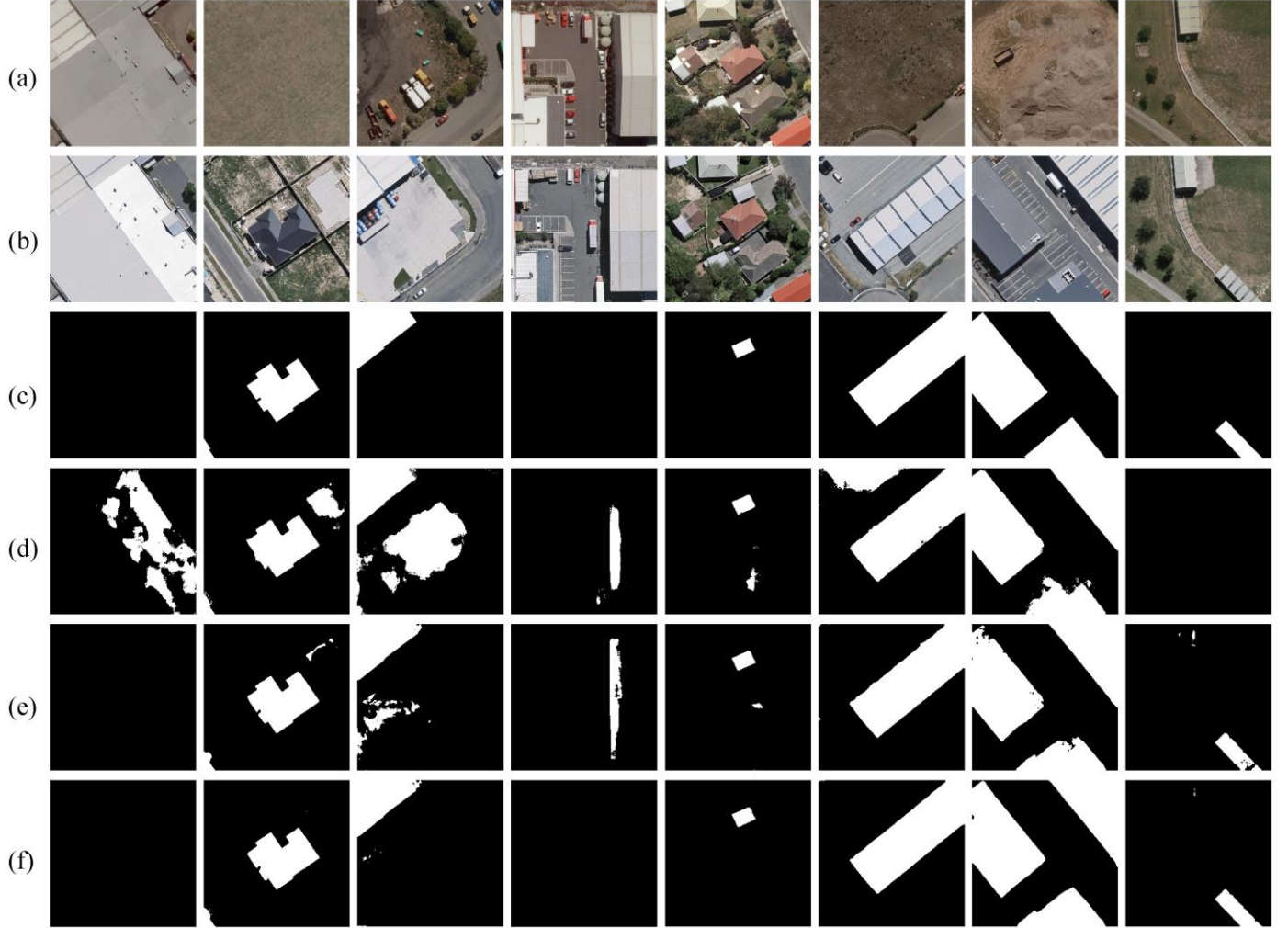


Fig. 6. Visualized change maps of the ablation studies for IA and FA modules. Images from left to right are (a) pre-event images, (b) post-event images, (c) ground truth, (d) the results of SNUNet, (e) the results of SNUNet + IA, (f) the results of SNUNet + IA + FA. Both IA and FA help to reduce false-positive predictions and generate fine details for the changed regions. The best performance is achieved when combining the baseline model with IA and FA.

4.4.2 Impact of Different Combinations of Bi-temporal Images

Different from general domain adaptation tasks [39][40][41] where only source-domain labels are available, for cross-domain change detection, the transformed bi-temporal images are still considered sharing the same annotations of changed regions, making it possible to adopt information from different domains for predictions. On the other hand, the generated bi-temporal images suffer from information loss more or less,

thus using only one domain bi-temporal images to train the change detection model would underutilize the image information. Therefore, we further explore the impact of different combinations of bi-temporal images.

Intuitively, we mainly experiment on three pairs of bi-temporal images, *i.e.* the original (I_{pre}, I_{post}) , $(I_{pre}, I_{post \rightarrow pre}) \in PrD$ and $(I_{pre \rightarrow post}, I_{post}) \in PoD$, which results in seven different combinations in total. We present the results in Table 3 and visualize the change maps in Fig. 7 for comparison. As observed, when only using one pair of bi-temporal images, the performance is $(I_{pre}, I_{post}) < (I_{pre}, I_{post \rightarrow pre}) < (I_{pre \rightarrow post}, I_{post})$, which proves that relieving appearance differences contributes to cross-domain change detection. If we combine two or more pairs of bi-temporal images to extract feature maps, the performance shows consistent improvements. When exploiting all three pairs of bi-temporal images, we obtain the best performance on the WHU building dataset with an *F1-score* of 92.36%, which is 6.85% higher than the baseline. Here we emphasize that incorporating the original bi-temporal images (I_{pre}, I_{post}) can also benefit change detection, because they contain all available information. Another interesting observation is that, if one pair of bi-temporal images obtains higher scores alone, such bi-temporal images can bring more obvious improvements when combined with other pairs. This provides a guidance to select proper combinations of bi-temporal images.

Table 3. Comparison of different combinations of bi-temporal images on WHU building dataset.

| $I_{pre} + I_{post}$ | $I_{pre} + I_{post \rightarrow pre}$ | $I_{pre \rightarrow post} + I_{post}$ | P (%) | R (%) | F (%) |
|----------------------|--------------------------------------|---------------------------------------|--------------|--------------|--------------|
| ✓ | ✓ | ✓ | 82.12 | 89.19 | 85.51 |
| | | | 87.62 | 86.94 | 87.28 |
| | | | 92.10 | 90.19 | 91.14 |
| ✓ | ✓ | ✓ | 87.28 | 88.09 | 87.68 |
| | ✓ | | 92.35 | 90.76 | 91.55 |
| ✓ | ✓ | ✓ | 91.91 | 90.62 | 91.26 |
| | ✓ | ✓ | 93.85 | 90.91 | 92.36 |

Moreover, though we achieve the best performance with the aforementioned combination of three bi-temporal images, we highlight that not all pairs of bi-temporal images as well as generated ones can constantly boost the performance. We also conducted experiments combining $(I_{pre \rightarrow post}, I_{post \rightarrow pre})$ and

possible combinations of reconstructed bi-temporal images ($I_{pre \rightarrow post \rightarrow pre}$, *) and ($I_{post \rightarrow pre \rightarrow post}$, *), but the performance of the change detection model was even worse than that of the original bi-temporal images. The reason would be that, those bi-temporal images suffer from information loss after iterative image-to-image transformation, which is harmful for the final change prediction.

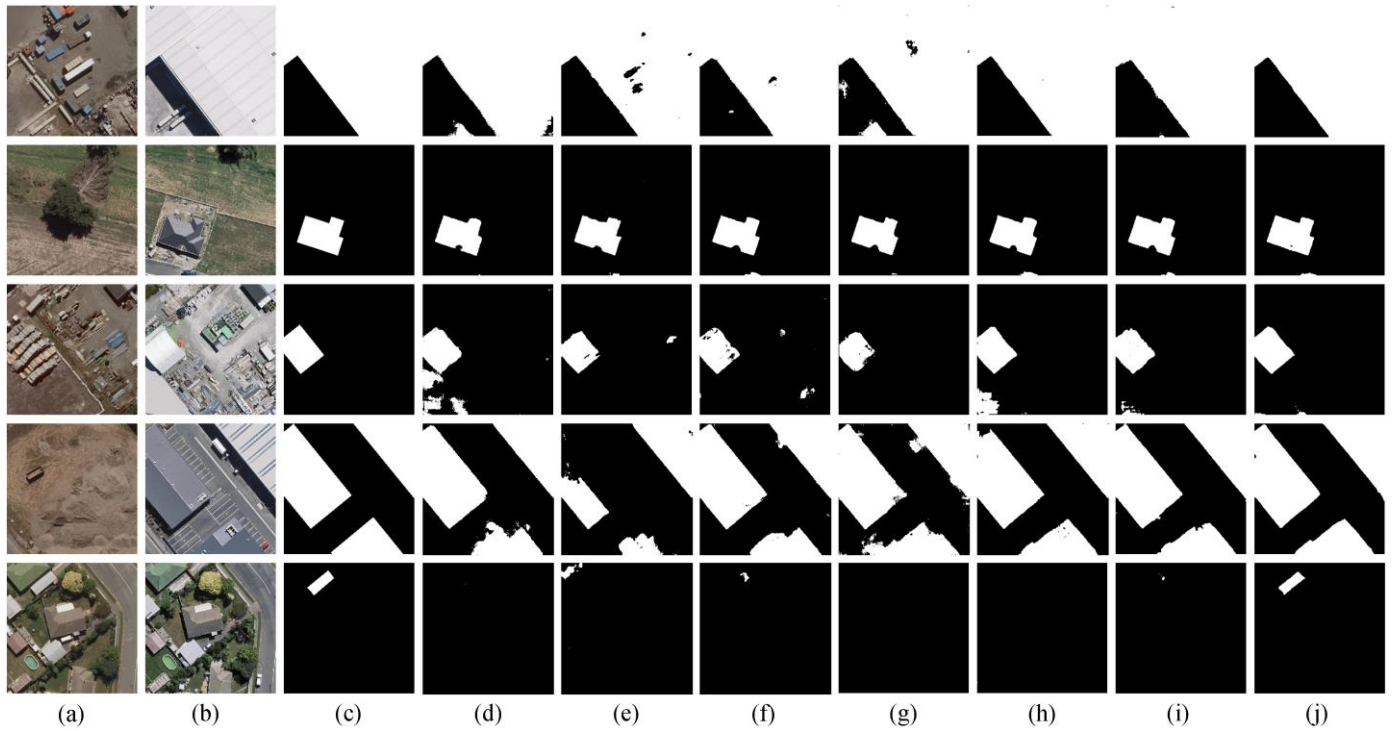


Fig. 7. Comparison of visualized change maps produced by different combinations of bi-temporal images. For simplicity, we denote bi-temporal images of (I_{pre}, I_{post}) , $(I_{pre}, I_{post \rightarrow pre})$ and $(I_{pre \rightarrow post}, I_{post})$ as I, II and III, respectively. Images from left to right are (a) pre-event images, (b) post-event images, (c) ground truth, the results of (d) I, (e) II, (f) III, (g) I + II, (h) I + III, (i) II + III, and (j) I + II + III, respectively.

4.4.3 Discussion of Different Fusion Strategies

Since we obtain three groups of domain-invariant feature maps after feeding three pairs of bi-temporal images into the feature adaptation module, we are curious about how to integrate these feature maps can produce better results. Here we explore two different fusion strategies, *i.e.*, output fusion and feature fusion, which are widely used in the computer vision community [47]-[49]. Output fusion refers to first predicting change map for each features of bi-temporal images and then integrating the results, while feature fusion integrates all feature maps for the final prediction. As shown in Table 4, feature fusion yields an *F1-score* of 92.36%, which is 0.5% higher than the output fusion. As shown in Fig. 8, we observe feature fusion can

discriminate detailed changes of the buildings and effectively prevent false positive predictions. We consider that feature fusion can better utilize the image information from different domains and compensate for each other, which formulates more expressive representations. Therefore, we employ feature fusion in our FA module, where three groups of feature maps from different domains are concatenated first and then fused to predict the final change map.

Table 4. Comparison of different fusion strategies on WHU building dataset.

| Fusion Strategy | P (%) | R (%) | F (%) |
|-----------------|--------------|--------------|--------------|
| output fusion | 93.21 | 90.55 | 91.86 |
| feature fusion | 93.85 | 90.91 | 92.36 |

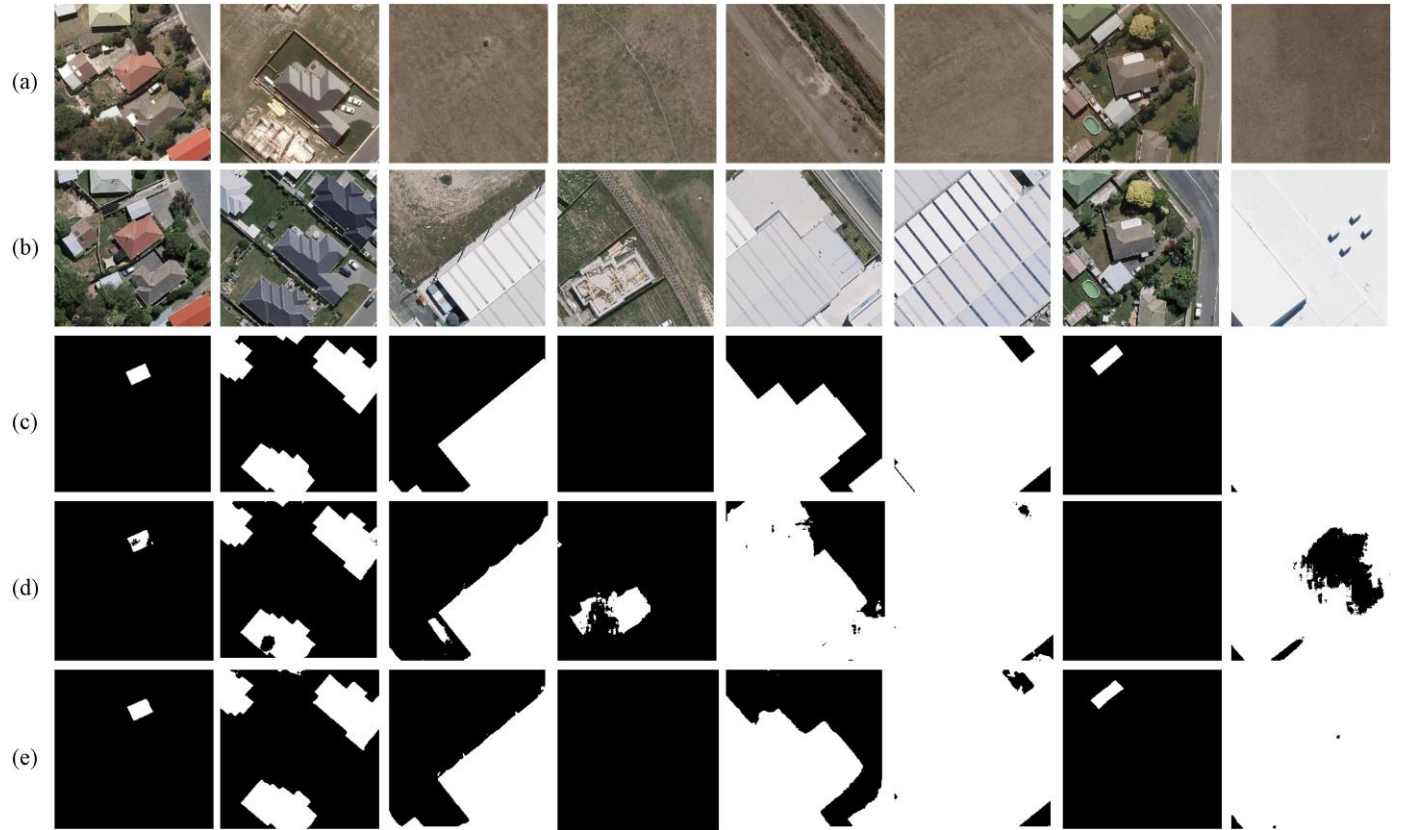


Fig. 8. Comparison of the change maps with different fusion strategies. Images from top to bottom are (a) pre-event images, (b) post-event images, (c) ground truth, (d) the results of output fusion, and (e) the results of feature fusion, respectively. Feature fusion shows to be more powerful in capturing semantic information than output fusion, producing complete change regions with accurate boundaries owing to integrated representations.

5 Conclusion

In this paper, we propose a novel end-to-end supervised domain adaptation framework, *i.e.*, SDACD, which can be easily incorporated with non-domain adaptation networks to tackle challenging cross-domain change detection on very high-resolution remote sensing images. The proposed IA module leverages generative adversarial networks to realize cross-domain image-to-image transformation, which aligns the appearance of bi-temporal images. To further reduce the remaining domain gap, we introduce an FA module, which extracts domain-invariant features from different domains for feature alignment, and we integrate feature maps from all domains for the final change prediction. Our experiments show the superiority of our framework in overcoming domain shift, which achieves the new state-of-the-art *F1-score* of 97.34% and 92.36% on CDD and WHU building datasets, respectively. More importantly, our method provides a general solution with great potential, capable of bringing consistent increments to existing change detection methods.

Acknowledgments

This work was supported in part by National Natural Science Foundation of China under Grant 62076186 and 61822113, and in part by Science and Technology Major Project of Hubei Province (Next-Generation AI Technologies) under Grant 2019AEA170. The numerical calculations in this paper have been done on the supercomputing system in the Supercomputing Center of Wuhan University.

References

- [1] Haobo Lyu, Hui Lu, Lichao Mou, Wenyu Li, Jonathon Wright, Xuecao Li, Xinlu Li, Xiao Xiang Zhu, Jie Wang, Le Yu, Peng Gong. 2018. Long-term annual mapping of four cities on different continents by applying a deep information learning method to landsat data. *Remote Sensing* 10, 3 (2018), 471.
- [2] Yunhao Gao, Feng Gao, Junyu Dong, and Shengke Wang. 2019. Transferred deep learning for sea ice change detection from synthetic-aperture radar images. *IEEE Geoscience and Remote Sensing Letters* 16, 10 (2019), 1655–1659.
- [3] Sudipan Saha, Francesca Bovolo, and Lorenzo Bruzzone. 2018. Destroyed-buildings detection from VHR SAR images using deep features. In *Image and Signal Processing for Remote Sensing XXIV*, Vol. 10789. International Society for Optics and Photonics, 107890Z.
- [4] William A Malila. 1980. Change vector analysis: an approach for detecting forest changes with Landsat. In *LARS symposia*. 385.
- [5] JS Deng, K Wang, YH Deng, and GJ Qi. 2008. PCA-based land-use change detection and analysis using multitemporal and multisensor satellite data. *International Journal of Remote Sensing* 29, 16 (2008), 4823–4838.

[6] Allan Aasbjerg Nielsen. 2007. The regularized iteratively reweighted MAD method for change detection in multi-and hyperspectral data. *IEEE Transactions on Image processing* 16, 2 (2007), 463–478.

[7] Prashanth R Marpu, Paolo Gamba, and Morton J Canty. 2011. Improving change detection results of IR-MAD by eliminating strong changes. *IEEE Geoscience and Remote Sensing Letters* 8, 4 (2011), 799–803.

[8] Chen Wu, Bo Du, Xiaohui Cui, and Liangpei Zhang. 2017. A post-classification change detection method based on iterative slow feature analysis and Bayesian soft fusion. *Remote Sensing of Environment* 199 (2017), 241–255.

[9] Ashish Ghosh, Niladri Shekhar Mishra, and Susmita Ghosh. 2011. Fuzzy clustering algorithms for unsupervised change detection in remote sensing images. *Information Sciences* 181, 4 (2011), 699–715.

[10] Konrad J Wessels, Frans Van den Bergh, David P Roy, Brian P Salmon, Karen C Steenkamp, Bryan MacAlister, Derick Swanepoel, and Debbie Jewitt. 2016. Rapid land cover map updates using change detection and robust random forest classifiers. *Remote Sensing* 8, 11 (2016), 888.

[11] Hassiba Nemmour and Youcef Chibani. 2006. Multiple support vector machines for land cover change detection: An application for mapping urban extensions. *ISPRS Journal of Photogrammetry and Remote Sensing* 61, 2 (2006), 125–133.

[12] Jungho Im and John R Jensen. 2005. A change detection model based on neighborhood correlation image analysis and decision tree classification. *Remote Sensing of Environment* 99, 3 (2005), 326–340.

[13] Wenzhong Shi, Min Zhang, Rui Zhang, Shanxiong Chen, and Zhao Zhan. 2020. Change detection based on artificial intelligence: State-of-the-art and challenges. *Remote Sensing* 12, 10 (2020), 1688.

[14] Hao Chen and Zhenwei Shi. 2020. A spatial-temporal attention-based method and a new dataset for remote sensing image change detection. *Remote Sensing* 12, 10 (2020), 1662.

[15] Jie Chen, Ziyang Yuan, Jian Peng, Li Chen, Haozhe Huang, Jiawei Zhu, Yu Liu, and Haifeng Li. 2020. DASNet: Dual attentive fully convolutional siamese networks for change detection in high-resolution satellite images. *IEEE Journal of Selected Topics in Applied Earth Observations and Remote Sensing* 14 (2020), 1194–1206.

[16] Sheng Fang, Kaiyu Li, Jinyuan Shao, and Zhe Li. 2021. SNUNet-CD: A densely connected siamese network for change detection of VHR images. *IEEE Geoscience and Remote Sensing Letters* 19 (2021), 1–5.

[17] Rodrigo Caye Daudt, Bertr Le Saux, and Alexandre Boulch. 2018. Fully convolutional siamese networks for change detection. In *2018 25th IEEE International Conference on Image Processing (ICIP)*. IEEE, 4063–4067.

[18] Qian Shi, Mengxi Liu, Shengchen Li, Xiaoping Liu, Fei Wang, and Liangpei Zhang. 2021. A deeply supervised attention metric-based network and an open aerial image dataset for remote sensing change detection. *IEEE Transactions on Geoscience and Remote Sensing* (2021).

[19] Moyang Wang, Kun Tan, Xiuping Jia, Xue Wang, and Yu Chen. 2020. A deep siamese network with hybrid convolutional feature extraction module for change detection based on multi-sensor remote sensing images. *Remote Sensing* 12, 2 (2020), 205.

[20] Bin Hou, Qingjie Liu, Heng Wang, and Yunhong Wang. 2019. From W-Net to CDGAN: Bitemporal change detection via deep learning techniques. *IEEE Transactions on Geoscience and Remote Sensing* 58, 3 (2019), 1790–1802.

[21] Min Zhang and Wenzhong Shi. 2020. A feature difference convolutional neural network-based change detection method. *IEEE Transactions on Geoscience and Remote Sensing* 58, 10 (2020), 7232–7246.

[22] Chenxiao Zhang, Peng Yue, Deodato Tapete, Liangcun Jiang, Boyi Shangguan, Li Huang, and Guangchao Liu. 2020. A deeply supervised image fusion network for change detection in high resolution bi-temporal remote sensing images. *ISPRS Journal of Photogrammetry and Remote Sensing* 166 (2020), 183–200.

[23] Yi Liu, Chao Pang, Zongqian Zhan, Xiaomeng Zhang, and Xue Yang. 2020. Building change detection for remote sensing images using a dual-task constrained deep siamese convolutional network model. *IEEE Geoscience and Remote Sensing Letters* 18, 5 (2020), 811–815.

[24] Hao Chen, Zipeng Qi, and Zhenwei Shi. 2021. Remote sensing image change detection with transformers. *IEEE Transactions on Geoscience and Remote Sensing* (2021).

[25] MA Lebedev, Yu V Vizilter, OV Vygolov, VA Knyaz, and A Yu Rubis. 2018. CHANGE DETECTION IN REMOTE SENSING IMAGES USING CONDITIONAL ADVERSARIAL NETWORKS. *International Archives of the Photogrammetry, Remote Sensing & Spatial Information Sciences* 42, 2 (2018).

[26] Shunping Ji, Shiqing Wei, and Meng Lu. 2018. Fully convolutional networks for multisource building extraction from an open aerial and satellite imagery data set. *IEEE Transactions on Geoscience and Remote Sensing* 57, 1 (2018), 574–586.

[27] Hui Zhang, Maoguo Gong, Puzhao Zhang, Linzhi Su, and Jiao Shi. 2016. Feature-level change detection using deep representation and feature change analysis for multispectral imagery. *IEEE Geoscience and Remote Sensing Letters* 13, 11 (2016), 1666–1670.

[28] Lichao Mou, Lorenzo Bruzzone, and Xiao Xiang Zhu. 2018. Learning spectral-spatial-temporal features via a recurrent convolutional neural network for change detection in multispectral imagery. *IEEE Transactions on Geoscience and Remote Sensing* 57, 2 (2018), 924–935.

[29] Faiz Rahman, Bhavan Vasu, Jared Van Cor, John Kerekes, and Andreas Savakis. 2018. Siamese network with multi-level features for patch-based change detection in satellite imagery. In *2018 IEEE Global Conference on Signal and Information Processing (GlobalSIP)*. IEEE, 958–962.

[30] Qi Wang, Zhenghang Yuan, Qian Du, and Xuelong Li. 2018. GETNET: A general end-to-end 2-D CNN framework for hyperspectral image change detection. *IEEE Transactions on Geoscience and Remote Sensing* 57, 1 (2018), 3–13.

[31] Hongyan Zhang, Manhui Lin, Guangyi Yang, and Liangpei Zhang. 2021. Escnet: An end-to-end superpixel-enhanced change detection network for very-high-resolution remote sensing images. *IEEE Transactions on Neural Networks and Learning Systems* (2021).

[32] Zhi Zheng, Yi Wan, Yongjun Zhang, Sizhe Xiang, Daifeng Peng, and Bin Zhang. 2021. CLNet: Cross-layer convolutional neural network for change detection in optical remote sensing imagery. *ISPRS Journal of Photogrammetry and Remote Sensing* 175 (2021), 247–267.

[33] Daifeng Peng, Lorenzo Bruzzone, Yongjun Zhang, Haiyan Guan, Haiyong Ding, and Xu Huang. 2020. SemiCDNet: A semisupervised convolutional neural network for change detection in high resolution remote-sensing images. *IEEE Transactions on Geoscience and Remote Sensing* 59, 7 (2020), 5891–5906.

[34] Olaf Ronneberger, Philipp Fischer, and Thomas Brox. 2015. U-net: Convolutional networks for biomedical image segmentation. In *International Conference on Medical Image Computing and Computer-Assisted Intervention*. Springer, 234–241.

[35] Zongwei Zhou, Md Mahfuzur Rahman Siddiquee, Nima Tajbakhsh, and Jianming Liang. 2018. Unet++: A nested u-net architecture for medical image segmentation. In *Deep Learning in Medical Image Analysis and Multimodal Learning for Clinical Decision Support*. Springer, 3–11.

[36] Bo Fang, Li Pan, and Rong Kou. 2019. Dual learning-based siamese framework for change detection using bi-temporal VHR optical remote sensing images. *Remote Sensing* 11, 11 (2019), 1292.

[37] Rong Kou, Bo Fang, Gang Chen, and Lizhe Wang. 2020. Progressive domain adaptation for change detection using season-varying remote sensing images. *Remote Sensing* 12, 22 (2020), 3815.

[38] Ian Goodfellow, Jean Pouget-Abadie, Mehdi Mirza, Bing Xu, David Warde-Farley, Sherjil Ozair, Aaron Courville, and Yoshua Bengio. 2014. Generative adversarial nets. *Advances in Neural Information Processing Systems* 27 (2014).

[39] Jun-Yan Zhu, Taesung Park, Phillip Isola, and Alexei A Efros. 2017. Unpaired image-to-image translation using cycle-consistent adversarial networks. In *Proceedings of the IEEE International Conference on Computer Vision*. 2223–2232.

[40] Judy Hoffman, Eric Tzeng, Taesung Park, Jun-Yan Zhu, Phillip Isola, Kate Saenko, Alexei Efros, and Trevor Darrell. 2018. Cycada: Cycle-consistent adversarial domain adaptation. In *International Conference on Machine Learning*. PMLR, 1989–1998.

[41] Liangchen Song, Yonghao Xu, Lefei Zhang, Bo Du, Qian Zhang, and Xinggang Wang. 2020. Learning from synthetic images via active pseudo-labeling. *IEEE Transactions on Image Processing* 29 (2020), 6452–6465.

[42] Yaroslav Ganin and Victor Lempitsky. 2015. Unsupervised domain adaptation by backpropagation. In *International Conference on Machine Learning*. PMLR, 1180–1189.

[43] Eric Tzeng, Judy Hoffman, Kate Saenko, and Trevor Darrell. 2017. Adversarial discriminative domain adaptation. In *Proceedings of the IEEE Conference on Computer Vision and Pattern Recognition*. 7167–7176.

[44] Ximei Wang, Liang Li, Weirui Ye, Mingsheng Long, and Jianmin Wang. 2019. Transferable attention for domain adaptation. In *Proceedings of the AAAI Conference on Artificial Intelligence*, Vol. 33. 5345–5352.

[45] Cheng Chen, Qi Dou, Hao Chen, Jing Qin, and Pheng-Ann Heng. 2019. Synergistic image and feature adaptation: Towards cross-modality domain adaptation for medical image segmentation. In *Proceedings of the AAAI Conference on Artificial Intelligence*, Vol. 33. 865–872.

[46] Yi-Hsuan Tsai, Wei-Chih Hung, Samuel Schulter, Kihyuk Sohn, Ming-Hsuan Yang, and Manmohan Chandraker. 2018. Learning to adapt structured output space for semantic segmentation. In *Proceedings of the IEEE Conference on Computer Vision and Pattern Recognition*. 7472–7481.

[47] Joseph Redmon and Ali Farhadi. 2018. Yolov3: An incremental improvement. *arXiv preprint arXiv:1804.02767* (2018).

[48] Tao Kong, Anbang Yao, Yurong Chen, and Fuchun Sun. 2016. Hypernet: Towards accurate region proposal generation and joint object detection. In *Proceedings of the IEEE Conference on Computer Vision and Pattern Recognition*. 845–853.

[49] Wei Liu, Dragomir Anguelov, Dumitru Erhan, Christian Szegedy, Scott Reed, Cheng-Yang Fu, and Alexander C Berg. 2016. Ssd: Single shot multibox detector. In *European Conference on Computer Vision*. Springer, 21–37.